

1 **Vertical structure of biomass burning aerosol transported over**
2 **the southeast Atlantic Ocean**

3 Harshvardhan Harshvardhan¹, Richard Ferrare², Sharon Burton², Johnathan Hair², Chris
4 Hostetler², David Harper², Anthony Cook², Marta Fenn³, Amy Jo Scarino³, Eduard Chemyakin³,
5 Detlef Müller⁴

6 ¹Purdue University, West Lafayette, IN, United States

7 ²NASA Langley Research Center, Hampton, VA, United States

8 ³Science Systems and Applications, Inc./NASA Langley Research Center, Hampton, VA, United States

9 ⁴University of Hertfordshire, Hatfield, Hertfordshire, United Kingdom

10 *Correspondence to:* H. Harshvardhan (harshvar@purdue.edu)

11 **Abstract.** Biomass burning in southwestern Africa produces smoke plumes that are transported over the Atlantic
12 Ocean and overlie vast regions of stratocumulus clouds. This aerosol layer contributes to direct and indirect radiative
13 forcing of the atmosphere in this region, particularly during the months of August, September and October. There was
14 a multi-year international campaign to study this aerosol and its interactions with clouds. Here we report on the
15 evolution of aerosol distributions and properties as measured by the airborne high spectral resolution lidar (HSRL-2)
16 during the ORACLES (Observations of Aerosols above Clouds and their intEractionS) campaign in September 2016.
17 The NASA Langley HSRL-2 instrument was flown on the NASA ER-2 aircraft for several days in September 2016.
18 Data were aggregated at two pairs of $2^\circ \times 2^\circ$ grid boxes to examine the evolution of the vertical profile of aerosol
19 properties during transport over the ocean. Results showed that the structure of the profile of aerosol extinction and
20 microphysical properties is maintained over a one to two-day time scale. In the 3-5 km altitude range, 95% of the
21 aerosol extinction was contributed by particles in the 0.05-0.50 μm radius size range, with the aerosol in this size
22 range having an average effective radius of 0.16 μm . This indicates that there is essentially no scavenging or dry
23 deposition at these altitudes. Moreover, there is very little day to day variation in these properties, such that time
24 sampling as happens in such campaigns, may be representative of longer periods such as monthly means. Below 3 km
25 there is considerable mixing with larger aerosol, most likely continental source near land. Furthermore, these
26 measurements indicated that there was often a distinct gap between the bottom of the aerosol layer and cloud tops at
27 the selected locations as evidenced by a layer of several hundred meters that contained relatively low aerosol extinction
28 values above the clouds.

29 **1 Introduction**

30 Aerosols are often considered as the most confounding element in the climate system when simulating parameters of
31 the Earth's current climate. Their interaction with clouds makes the problem extremely complicated. The general topic
32 of aerosol-cloud interaction has been of great interest in the scientific community: to quote the report of the
33 Intergovernmental Panel on Climate Change (IPCC AR5) "Clouds and aerosols continue to contribute the largest
34 uncertainty to estimates and interpretations of the Earth's changing energy budget" (Boucher et al., 2013).

35 In the context of these interactions, the interplay of biomass burning (BB) aerosol and the stratocumulus clouds in
36 the Southeast (SE) Atlantic is unique and crucial to the estimates of the energy budget of the region. This BB aerosol
37 arises from the seasonal burning (July-October) of agricultural residue in the southwestern African Savannah and
38 traverses large distances westward over the SE Atlantic Ocean. Unlike the aerosol from industrial activity and biofuels
39 that intermingle with clouds in many regions (Ramanathan et al., 2001; Mechoso et al., 2013), these optically thick
40 BB aerosol layers overlay vast stretches of marine stratus cloud in the SE Atlantic (Chand et al., 2009; Wilcox, 2010;
41 Adebiyi et al., 2015) where they have a direct radiative effect. The BB aerosol can also act as nuclei for cloud droplets
42 and so cause a potentially significant cloud albedo effect. Observations and modelling studies of such interactions in
43 the Southeast Atlantic and southern Africa regions [include](#) Diamond et al. (2018), Kacarab et al. (2020), [Mallet et al.](#)
44 [\(2020\)](#) and Gupta et al. (2021). There is also some evidence that aerosol can alter the thermodynamics of cloud
45 formation through semi-direct effects (Sakaeda et al., 2011). Studies using high resolution limited area models have
46 shown a variety of effects, including stratus to cumulus transition resulting from these interactions (Yamaguchi et al.,
47 2015; Gordon et al., 2018; Lu et al., 2018). The semi-direct effect has also been shown to be important in a limited
48 time run of a global model (Das et al., 2020).

Deleted: are in

49 During the course of its transport over the Atlantic basin, the dense BB aerosol layer affects the underlying clouds
50 and Earth's radiative balance in multiple ways. It exerts a direct radiative forcing (DRF) [by scattering and absorbing](#)
51 [solar radiation in the atmosphere; when clouds are present, these aerosols absorb](#) incoming solar radiation along with
52 the radiation reflected by the underlying cloud surface (Chand et al., 2009; Meyer et al., 2013; Zhang et al., 2016).
53 Simultaneously, depending on the relative vertical location of the aerosol with respect to the cloud deck, the cloud
54 cover (fraction) or liquid water path may increase or decrease in response to heating of surrounding air masses due to
55 aerosol absorption and subsequent changes in atmospheric stability, the semi-direct forcing (Sakaeda et al., 2011;
56 Wilcox, 2012; Das et al., 2020). [Observations at Ascension Island show that daytime cloud cover and relative humidity](#)
57 [are lower when there is more smoke in the marine boundary layer \(Zhang and Zuidema, 2019\).](#) Moreover, as the
58 marine boundary layer (MBL) deepens farther offshore and north of 5°S, subsiding aerosol particles become entrained
59 into the MBL and interact with the clouds as cloud condensation nuclei to affect their microphysics (indirect forcing)
60 (Costantino and Breon, 2013; Painemal et al., 2014).

Deleted: on the atmosphere by absorbing the

Deleted:

61 In the context of simulating the above alluded aerosol radiative effects, it is vital that aerosol-cloud overlap
62 characteristics are accurately represented within the models. The quantification of these aerosol-cloud overlap
63 characteristics in the models is necessary for a variety of reasons. For example, previous studies have found that the
64 sign and magnitude of DRF of absorbing aerosol above clouds (AAC) critically depends upon the reflectance and
65 coverage of the underlying cloud surfaces along with the optical properties, composition and size distribution of the
66 overlying aerosols (Keil and Haywood, 2003; Chand et al., 2009). Additionally, the magnitude and sign of the aerosol
67 semi-direct effects are quite sensitive to the vertical distribution of aerosols, especially with respect to the vertical
68 location of clouds (Penner et al., 2003; McFarquhar and Wang, 2006; Koch and Del Genio, 2010).

69 Here we address the evolution of the vertical properties of BB aerosol as it travels in the marine environment after
70 leaving the African land mass. Section 2 identifies the field campaign and specifies the geographic region selected for
71 the analysis and rationale for that choice. Section 3 describes the attributes of the instrument and key parameters

75 related to the aerosol that can be extracted from the measurements. Section 4 presents the results followed by a
76 summary and conclusion in section 5.

77 **2 Field Campaigns**

78 The concerns mentioned above were the driving force behind plans for several international multi-year field
79 campaigns; ORACLES (Observations of Aerosols above Clouds and their intEractiOnS, Redemann et al., 2021),
80 CLARIFY-2017 (CLoud-Aerosol-Radiation Interactions and Forcing for Year 2017, Haywood et al., 2021), and
81 LASIC (Layered Atlantic Smoke Interactions with Clouds, Zuidema et al., 2016, 2018). A key component of the
82 September 2016 NASA ORACLES Intensive Observation Period (IOP) was the vertical profiling of aerosol properties
83 measured by an airborne lidar, the NASA Langley High Spectral Resolution Lidar-2, HSRL-2 (Burton et al., 2018),
84 on-board the NASA ER-2, which was based in Walvis Bay, Namibia, for operations during 2016.the deployment
85 covered in this study. In the following two years, the instrument was on-board the P-3 flying out of São Tomé. The
86 siting and flight tracks chosen ensured adequate coverage of the seasonal BB aerosol.

87 **2.1 Meteorology**

88 The September monthly mean meteorological situation is shown in Fig. 1 from MERRA2 reanalysis (Buchard et
89 al., 2017; Randles et al., 2017) along with locations of relevant sites. A thorough meteorological analysis for all
90 ORACLES deployments is provided in Ryoo et al. (2021). For the period under consideration here, they found that
91 the African Easterly Jet-South (AEJ-S), fast moving zonal easterlies centered on 650 hPa around 5-15°S, was active
92 and corresponded closely to the long-term climatology. Fig. 2 shows 650 hPa winds from MERRA2 reanalysis at the
93 beginning, at the end, and on two intermediate days during which HSRL-2 measurements were made. ER-2 flight
94 tracks during the September 2016 IOP are shown in Fig. 3. Note that flights were primarily confined to within roughly
95 1000 km of the African coast with only the 22 September flight venturing further. Flights such as executed during the
96 IOP are unable to follow air parcels in a Lagrangian fashion to examine the evolution of smoke plumes. Here we
97 provide an alternate framework by which to study evolving aerosol properties in an average sense. In order to establish
98 average characteristics of the BB smoke plume as it travels over the ocean, we have chosen five grid boxes of two-
99 degree latitude and longitude on a side at various distances from the source and aggregated observations. The choice
100 of grid boxes was based on the availability of data from the flights (Fig. 3) and the general direction of transport of
101 the smoke as evidenced by the wind fields in Fig. 2. The grid boxes so chosen are marked on Figs. 2 and 3 and the
102 rationale for the choice is explained below.

103 Figure 4 shows 48-hour backward trajectory frequency analyses at 3.5 km, roughly the central altitude of the plume,
104 using NOAA HYSPLIT trajectory calculations (https://www.ready.noaa.gov/HYSPLIT_traj.php) which were carried
105 out using archived GDAS 0.5-degree meteorology (Stein et al., 2015). The frequency distribution is a 48-hour history
106 of the paths taken by air parcels arriving at the grid boxes marked A and C at 3500 m altitude. The time period of the
107 frequency analyses covers the entire period during which HSRL-2 measurements were made, 12-24 September 2016.

Deleted: IOPs

Deleted:

110 The selected grid box pairs indicate that Box A receives aerosol that has earlier crossed Box B and Box C is downwind
111 of Box D; boxes B and D receive aerosol directly from BB sources on land. The grid box pairs A/B and C/D can
112 therefore provide information on the evolution of the microphysics and vertical distribution of BB aerosol plumes
113 after leaving the continent. This strategy is similar to that used in comparisons of models with observations for this
114 campaign by Shinozuka et al. (2020), who also showed that observations made on the sampled days were
115 representative of monthly means. In addition to the four boxes strongly influenced by smoke, a southern box, E, has
116 been chosen to provide a control contrast to the other areas in that it is influenced primarily by maritime air as seen
117 from Figs. 1 and 2.

118 **2.2 ORACLES 2016 IOP**

119 The days during the campaign that were included in the averaging procedure are shown in Table 1. Also included
120 is the typical time of the day when the measurements were made, a function of the flight pattern of the ER-2. The
121 number of lidar return profiles averaged for each grid box and statistics related to the backward trajectories are also
122 listed. These grid boxes contained aircraft tracks on multiple days during which trajectory analysis showed near-
123 uniform wind direction between 2.5 and 4.5 km altitude throughout the IOP. With the exception of the grid box
124 centered at 22° S, 9° E, all indicate flow from the source region of BB aerosol. Table 1 also lists the mean and standard
125 deviation of time duration in hours spent over water of air parcels arriving at 3500 m altitude at the grid box during
126 the averaging period. There is no entry for Box E since arriving air had a maritime source and did not originate from
127 land. It must be stressed that the duration is not calculated from the source region on land, which is distributed over a
128 large area of central Africa (e.g., Fig. 9 of Redemann et al., 2021) and cannot be uniquely identified with specific
129 observations made over the ocean. The plume has already been airborne over land for several hours (see Fig. 4) and
130 aerosol would have undergone transformations that occur at short time scales (Cappa et al., 2020). The duration was
131 calculated by running HYSPLIT backward trajectories of air parcels arriving every six hours starting at 0600 UTC on
132 the days of the first flight and ending at 1800 UTC on the days of the last flight of the averaging period and is shown
133 in some detail in Fig. 5, which essentially reflects the profile of the prevailing wind speeds. The inference is that BB
134 smoke at 3500 m altitude arrives at A on average about 30 h after passing B and arrives at C 35 h after passing D. The
135 change in selected aerosol properties as measured by the HSRL-2 during this travel in the marine environment provides
136 information on the evolution of the plume during this time period.

137 **3 HSRL-2**

138 The NASA LaRC HSRL-2 uses the HSRL technique to independently retrieve aerosol extinction and backscatter
139 (Shipley et al., 1983; Grund and Eloranta, 1991; She et al., 1992) without a priori assumptions on aerosol type or
140 extinction-to-backscatter ratio. By using the HSRL technique, HSRL-2, like its predecessor HSRL-1 (Hair et al.,
141 2008), provides accurate backscatter profiles even in situations where the lidar beam is attenuated by overlying cloud
142 or aerosol as long as it is not completely attenuated. The LaRC HSRL-2 employs the HSRL technique at 355 and 532

143 nm and the standard backscatter technique at 1064 nm. It also measures aerosol and cloud depolarization at all three
144 wavelengths. The HSRL-2 provides vertically resolved measurements of the following extensive and intensive aerosol
145 parameters below the aircraft (approximate archival horizontal, Δx , and vertical resolutions, Δz , are listed assuming
146 ER-2 cruise speed).

147 • *Extensive parameters*¹ – backscatter coefficient, β , at 355, 532 and 1064 nm ($\Delta x \sim 2$ km, $\Delta z \sim 15$ m); extinction
148 coefficient, α , at 355, and 532 nm ($\Delta x \sim 12$ km, $\Delta z \sim 300$ m); optical depth at 355 and 532 nm (integrating the profile
149 of extinction). The aerosol optical depth (AOD) is a critical quantity in discussions of the influence of aerosol on
150 climate (Boucher et al., 2013).

151 • *Intensive parameters* – extinction-to-backscatter ratio of aerosol, the Lidar Ratio, $S_a = \alpha_a / \beta_a$, at 355 and 532 nm
152 ($\Delta x \sim 12$ km, $\Delta z \sim 300$ m); depolarization, $\delta_a = \beta_a^\perp / \beta_a^l$, at 355, 532, and 1064 nm ($\Delta x \sim 2$ km, $\Delta z \sim 15$ m); and
153 aerosol backscatter wavelength dependence (i.e., Ångström exponent for aerosol backscatter – directly related to the
154 backscatter color ratio) for two wavelength pairs (355-532 and 532-1064 nm, $\Delta x \sim 2$ km, $\Delta z \sim 15$ m).

155 The overall systematic error associated with the backscatter calibration is estimated to be less than 5 % for the 355
156 and 532 nm channels and 20 % for 1064 nm (Burton et al., 2015). Under typical conditions, the total systematic error
157 for extinction is estimated to be less than 0.01 km^{-1} at 532 nm. The random errors for all aerosol products are typically
158 less than 10 % for the backscatter and depolarization ratios (Hair et al., 2008). Rogers et al. (2009) validated the HSRL
159 extinction coefficient profiles and found that the HSRL extinction profiles are within the typical state-of-the-art
160 systematic error at visible wavelengths (Schmid et al., 2006). Since HSRL-2 includes the capability to measure
161 backscatter at three wavelengths and extinction at two wavelengths, “ $3\beta+2\alpha$ ” microphysical retrieval algorithms
162 (Müller et al., 1999a, 1999b; Veselovskii et al., 2002) are used to retrieve height-resolved parameters such as aerosol
163 effective radius and number, surface and volume concentrations (Müller et al., 2014, Sawamura et al., 2016). Here we
164 restrict ourselves to the effective radius of the particles.

165 4 Results

166 In this study of the vertically resolved evolving properties of BB aerosol, we present key lidar measurements and
167 microphysical results obtained by performing the “ $3\beta+2\alpha$ ” retrieval mentioned in Section 3.

¹ By the term *extensive*, we refer to optical parameters, such as extinction, that are influenced by the amount (concentration) and type (size, composition, shape) of aerosol/cloud particles. *Intensive* properties, on the other hand, are those that depend only on the nature of the particles and not on their quantity or concentration, but rather depend only on aerosol type (Anderson et al., 2003).

170 **4.1 Lidar**

171 Vertical profiles averaged over the times of overflight in $2^\circ \times 2^\circ$ latitude/longitude boxes shown in Figure 3 on the
172 days given in Table 1 are for the following properties.

- 173 1. Aerosol Extinction at 532 nm, α_a , determined by aerosol number concentration, microphysical
174 properties and relative humidity
- 175 2. Backscatter Ångström exponent between 1064 and 532 nm, an indication of particle size.
- 176 3. Aerosol Depolarization at 532 nm, a measure of particle asphericity.
- 177 4. Aerosol extinction to backscatter ratio, the Lidar Ratio, at 532 nm, a marker for aerosol composition.

Deleted:

178 Inspection of the wind field at 650 hPa in Fig. 2 and backward trajectory frequency plots in Fig. 4 suggest that the
179 grid boxes chosen fit naturally into two pairs of tracks of the widespread BB aerosol field. The northern pair, identified
180 in Table 1 as A and B, centered around 10° S, are in a faster zonal track, whereas the grid boxes C and D are in a track
181 centered between $13-15^\circ$ S that is slightly slower and has a component from the north over a stretch of water (Fig. 2).
182 The two pairs can then provide information on the evolution of aerosol properties over a time scale of one to two days.
183 Figures 6-9 show the aerosol extinction, backscatter Ångström exponent, aerosol depolarization and Lidar Ratio for
184 the two pairs of grid boxes and Box E, which is [at the southern edge of the region](#) influenced by the BB aerosol. The
185 results presented are one-minute averages of independent 10 s vertical profiles for backscatter Ångström exponent
186 and depolarization and one-minute averages for extinction and lidar ratio profiles. From Table 1, the mean time elapsed
187 between B and A is 29.4 h and that between D and C is 34.9 h. It should be pointed out that parameter values shown
188 below the level of mean cloud top are averages of lidar returns through breaks in the stratus deck and are not relevant
189 for this study. If we use the low cut-off of an extinction coefficient of 15 Mm^{-1} to indicate an aerosol-free layer
190 (Shinozuka et al., 2020), then Fig. 6 indicates that the bulk of the smoke layers encountered at these distances from
191 land were separated from the cloud top, a feature more prevalent during the 2016 IOP than in 2017 and 2018
192 (Redemann et al., 2021).

Deleted: not significantly

193 The northern plume is a column of aerosol of relatively constant extinction from just above 2.5 km to 5 km while
194 the southern plume has a profile of extinction that increases nearly linearly with height from a minimum near the cloud
195 top to a maximum at 5 km (Fig. 6). The vertical structure of the aerosol profiles measured by HSRL-2 was compared
196 to water vapor profiles represented by the Modern-Era Retrospective analysis for Research and Applications, Version
197 2 (MERRA2) model. Pistone et al. (2021) explored the relationship between aerosols, CO, water vapor as measured
198 by ORACLES airborne in situ measurements and represented by models including MERRA2. They found the
199 MERRA2 water vapor profiles, like the measured water vapor profiles, exhibited a linear relationship with CO and
200 biomass burning plume strength; they also found that smoky, humid air produced by daytime convection over the
201 continent advected over the ocean and into the ORACLES study region. MERRA2 water vapor profiles produced at
202 three hourly increments and 72 pressure levels were interpolated to the times and locations of the HSRL-2 profiles.
203 Water vapor mixing ratio generally decreased significantly just above the PBL then increased for altitudes around 2
204 to 3 km before decreasing again. This behavior is generally consistent with the relationship between water vapor and
205 aerosol scattering reported by Pistone et al. (2021).

208 Figure 10 shows the median, 25th and 75th percentile relative humidity (RH) profiles computed by interpolating the
209 MERRA2 0.5-deg. 3-hourly humidity profiles to the locations and times of the HSRL-2 measurements. The profiles
210 typically show a more pronounced increase in RH with altitude that more closely follows the HSRL-2 measurements
211 of aerosol extinction profiles, although the MERRA2 profiles typically begin decreasing above 4 km whereas the
212 airborne in situ RH measurements and HSRL-2 aerosol extinction profiles begin decreasing above 5 km. Interestingly,
213 during three of the dates (Sept. 12, 16, 22) considerable portions of the smoke layers correspond to MERRA2 relative
214 humidity above 60-70%. This increase in RH with altitude could help explain at least some of the increase in aerosol
215 extinction with height observed in the HSRL-2 profiles of the C/D Box pair. Aerosol humidification often amplified
216 the increase in aerosol extinction by factors of 1.5 or more (Doherty et al., 2022).

217 The Ångström exponent (Fig. 7) and depolarization (Fig. 8) indicate the presence of fine spherical particles at the
218 top of the plume and increasing sizes towards the bottom. The Lidar Ratio (Fig. 9) above 3 km for the two pairs is
219 between 70 and 80 sr, suggesting strong absorption (Müller et al., 2019) but is considerably less and highly variable
220 in Box E and in the lower layers of the aerosol plume in Box D, where the smoke plume most likely has components
221 of continental aerosol such as dust and pollution typical of the nearby Namibian coast (Klopper et al., 2020). The most
222 striking feature of the results is the very small profile-to-profile variability of the intensive lidar parameters in the
223 upper two kilometers of the plume over the course of several days as evident from the range of values in the 25-75
224 percentile shaded grey in Figs. 7-9. This suggests strongly that the particles maintain their size, shape and absorbing
225 properties over the first few days of transport over the ocean. This result is of some importance for climate studies in
226 which the radiative properties of BB aerosol are input to the calculation of radiative forcing. Complex chain aggregates
227 as found near the source of fires (Pósfai et al., 2003, China et al., 2013) are typically not represented in climate models.
228 However, if the aerosol is already spherical and maintains its size over the time period of radiative interactions being
229 studied, then core-shell models of varying degrees of complexity could perhaps suffice (Zhang et al., 2020). The lower
230 portion of the plume containing larger BB aerosol particles is subject to mixing with marine and continental particles
231 from regions not affected by biomass burning and is highly variable in nature. This would be more difficult to model
232 but Fig. 6 shows that the aerosol extinction coefficient decreases rapidly at lower levels so errors in representation
233 may be acceptable.

234 **4.2 Microphysics**

235 The lidar measurements are inverted to obtain information regarding particle size. The inversion is performed on one-
236 minute averages of six independent 10 s backscatter profiles and one-minute average extinction profiles. Details of
237 the inversion process are in Müller et al. (2019) and references therein. The particle size distribution is represented
238 using a series of eight triangular basis functions that can represent both monomodal and bimodal size distributions
239 (*ibid*). Points to note are that the procedure makes the following assumptions: the particles are spherical and
240 homogeneous having wavelength-independent complex index of refraction. The low (< 5 %) values of depolarization
241 through most of the plume, shown in Fig. 8, suggests that the spherical assumption is justified. There is most likely
242 structure and inhomogeneity in the core of the particles, but current particle optical models are unable to incorporate

243 these complexities. Results from this inversion procedure have been compared to coincident airborne in situ particle
244 measurements. Müller et al. (2014) present results from a campaign off the northeast coast of the US showing that the
245 inversion results agree with in situ measurements of effective radius and also number, surface area and volume
246 concentration within error bars. Sawamura et al. (2017) report on campaigns in the wintertime San Joaquin Valley of
247 California and summertime near Houston, TX. They found high correlation and low bias in surface and volume
248 concentration in situ measurements relative to HSRL with the best agreement for submicron fine-mode aerosol, which
249 is most relevant to the current study. Müller et al. (2019) report retrievals and their uncertainty for one day in the
250 ORACLES campaign, 22 September 2016. Considering only optical data with strong signal-to-noise ratio, they
251 estimate retrieval errors are 25 % for number concentration. The relative uncertainty in effective radius for parts of
252 the flight track where particle size was nearly constant was below 20 %.

253 In order to help separate particles that have BB source from coarser particles of continental or marine origin, we
254 specify a Submicron Fraction (SMF) as the contribution to the extinction at 532 nm of particles in the radius range
255 0.05–0.50 μm (Anderson et al., 2005). Figure 11 shows the profiles of SMF for the five grid boxes and not surprisingly,
256 the bulk of the smoke plume, especially between 3 and 5 km contains aerosol almost entirely in the submicron range.
257 Below 3 km, at locations both near and further way from the coast, there is a marked increase in the fraction of larger
258 particles. The increase in depolarization (Fig. 8) at these lower levels and a decrease in the Lidar Ratio (Fig. 9) suggest
259 mixing with the aforementioned non-BB aerosol particles. However, the sharp decrease in extinction below 3 km (Fig.
260 6) indicates that their contribution to direct radiative effects would be minimal. Finally, Fig. 12 shows the vertical
261 profile of the effective radius of the SMF aerosol population. The effective radius is 0.16 μm with little variation
262 between 3 and 5 km. Of greater significance is that it remains very similar between the pairs of grid boxes along the
263 transport trajectory of the smoke. The retrieved effective radius is similar to the results presented by Müller et al.
264 (2014) for a mixture of urban aerosol and smoke. Their comparison with in situ measurements showed a slight
265 overestimate but within a standard deviation. The retrieved and in situ results also show that the particle size is uniform
266 with altitude even when the number concentration drops by a factor of three. Another set of prior comparisons of
267 HSRL-2 and in situ measurements is provided in Sawamura et al. (2017). Here again, the effective radius of the
268 submicron fraction of particles, 0.15 μm , is uniform with altitude, and comparable though biased slightly low
269 compared to in situ observations.

270 The effective radii of the SMF aerosols, which typically vary between 0.15 to 0.20 μm , are generally consistent
271 with the sizes reported previously for smoke aerosol in the ORACLES region. Haywood et al. (2021) provide a
272 composite of the aerosol sizes for biomass burning aerosol off the South African coast. These size distributions, which
273 were derived from airborne in situ measurements (Haywood et al., 2003; Peers et al., 2019; Wu et al., 2020), typically
274 correspond to SMF aerosol effective radii between 0.14–0.17 μm and were for the dry aerosol. As discussed in section
275 4.1, the RH on some days was above 60–70% so that effective radii under ambient conditions could be expected to be
276 somewhat higher than for the dry aerosol. Using measurements from an airborne Differential Aerosol Sizing and
277 Hygroscopicity Spectrometer Probe (DASH-SP), Shingler et al. (2016) quantified the size-resolved growth factors for
278 several aerosol types; they found that at RH~70–80%, particle diameters for biomass burning aerosols were about 15–
279 20% larger than for the dry aerosol. Xu et al. (2021) derived aerosol properties during the 2016 ORACLES mission

280 using an inversion algorithm that combined HSRL-2 and Research Scanning Polarimeter (RSP) remote sensing
281 measurements. These retrieved aerosol properties were then compared with those derived from airborne *in situ*
282 measurements. For measurements acquired on Sept. 12, 2016, the SMF aerosol effective radius derived from the
283 remote sensing measurements were generally between 0.12-0.15 μm and were only slightly (0.012 μm) higher than
284 the effective radii for the (dry) SMF aerosol derived from the airborne *in situ* size distribution measurements. This
285 suggests that some of this difference is associated with differences in RH between the remote sensing retrievals and
286 the *in situ* measurements.

Formatted: Font: (Default) Times New Roman, 10 pt

287 **5 Conclusions**

288 The results of the aggregated HSRL-2 profiles during the 2016 ORACLES IOP presented here show two main
289 findings. These are however limited to a brief period in the transport of BB smoke from continental Africa over marine
290 clouds in the Atlantic Ocean. This is a limitation of the 2016 campaign because the flight tracks remained within 1000
291 km of the coast. For the period of one to two days after crossing the land-ocean boundary, the fraction of all particles
292 that are in the submicron range in the main smoke plume between 3 and 5 km is around 95 %. The effective radius of
293 the submicron particles in this altitude interval is 0.16 μm and essentially constant with altitude. The particle size is
294 comparable to measured particle sizes in previous campaigns that sampled aerosol that was a mixture of urban haze
295 and smoke (Müller et al., 2014; Sawamura et al., 2017). Moreover, the shape of the median vertical profile of
296 extinction does not change during the first two days of transport over water suggesting the absence of dry deposition
297 and wet scavenging. The low (< 0.05) depolarization ratio of the submicron particles signifies that they are well coated
298 and the assumption of sphericity in the inversion procedure and models that estimate the radiative effects of aerosol
299 is justified. The BB aerosol mix with continental and marine aerosol at the base of the plume but during the September
300 2016 IOP this layer of mixed aerosol tended to have very low extinction coefficients suggesting low abundance and
301 there was often a distinct gap between the plume and the cloud tops.

302 The HSRL-2 instrument was also deployed in the 2017 and 2018 ORACLES campaigns but was deployed on the
303 NASA P-3 which often flew at low altitude to acquire *in situ* measurements of aerosols and clouds. Consequently, the
304 HSRL-2 was not able to make continuous measurements of the BB aerosol plumes in a manner similar as when
305 deployed on the ER-2. However, there are segments of the track that can provide similar information to the data
306 obtained in the 2016 campaign but for a different time period. Moreover, some flight tracks extended much further
307 from land (Doherty et al., 2021). Analysis of the later campaigns will provide information on the physical evolution
308 of aerosol that has aged for a longer period than is covered in this study.

309 **Data Management**

310 HSRL-2 optical data and retrieved inversion data are available at the NASA archive site
311 <https://espoarchive.nasa.gov/archive/browse/oracles/id8/ER2> and are permanently archived at
312 doi:10.5067/SUBORBITAL/ORACLES/ER2/2016_V1.

313 **Acknowledgements**

314 The lead author would like to thank NASA Langley Research Center for hosting him during a sabbatical when this
315 study was initiated. HSRL-2 participation in ORACLES was supported by NASA through the Earth Venture
316 Suborbital-2 (EVS-2) program (grant no. 13-EVS2-13-0028). Funding for this work was also provided by NASA
317 through the Radiation Sciences Program. We wish to thank the NASA ER-2 pilots and ground crew for their extensive
318 support during ORACLES.

319

320 **References**

321 Anderson, T. L., Charlson, R. J., Winker, D. M., Ogren, J. A., and Holmén, K.: Mesoscale variations of tropospheric
322 aerosols, *J. Atmos. Sci.*, 60(1), 119-136, 2003.

323 Anderson, T. L., Wu, Y., Chu, D. A., Schmid, B., Redemann, J., and Dubovik, O.: Testing the MODIS satellite
324 retrieval of aerosol fine-mode fraction, *J. Geophys. Res.*, 110, D18204, doi:10.1029/2005JD005978, 2005.

325 Adebiyi, A. A., Zuidema, P., Chang, I., Burton, S. P., and Cairns, B.: Mid-level clouds are frequent above the Southeast
326 Atlantic stratocumulus clouds, *Atmos. Chem. Phys.*, 20, 11025-11043, doi:10.5194/acp-20-11025-2020, 2020.

327 Boucher, O., Randall, D., Artaxo, P., Bretherton, C., Feingold, G., Forster, P., Kermanen, V.-M., Kondo, Y., Liao, H.,
328 Lohmann, U., Rasch, P., Sathesh, S. K., Sherwood, S., Stevens, B., and Zhang X.Y.: Clouds and Aerosols. In:
329 Climate Change 2013: The Physical Science Basis. Contribution of Working Group I to the Fifth Assessment Report
330 of the Intergovernmental Panel on Climate Change [Stocker, T. F., Qin, D., Plattner, G.-K., Tignor, M., Allen, S.
331 K., Boschung, J., Nauels, A., Xia, Y., Bex V., and Midgley, P. M. (eds.)]. Cambridge University Press, 2013.

332 Buchard, V., Randles, C. A., da Silva, A. M., Darmenov, A., Colarco, P. R., Govindaraju, R., Ferrare, R. A., Hair, J.,
333 Beyersdorf, A. J., Ziembka L. D., and Yu, H.: The MERRA-2 aerosol reanalysis, 1980 onwards Part II: Evaluation
334 and case studies, *J. Climate*, 30, 6851-6871, doi:10.1175/JCLI-D-16-0613.1, 2017.

335 Burton, S. P., Hostettler, C. A., Cook, A. L., Hair, J. W., Seaman, S., Scolar, S., Harper, D. B., Smith, J. A., Fenn, M.
336 A., Ferrare, R. A., Saide, P. E., Chemyakin, E. V., and Müller, D.: Calibration of a high spectral resolution lidar
337 using a Michelson interferometer with data examples from ORACLES, *Appl. Optics*, 57, 6061-6075, 2018.

338 Burton, S. P., Hair, J. W., Kahnert, M., Ferrare, R. A., Hostettler, C. A., Cook, A. L., Harper, D. B., Berkoff, T. A.,
339 Seaman, S. T., Collins, J. E., Fenn, M. A., and Rogers, R. R.: Observations of the spectral dependence of linear
340 particle depolarization ratio of aerosols using NASA Langley airborne High Spectral Resolution Lidar, *Atmos.
341 Chem. Phys.*, 15, 13453-13473, doi.org/10.5194/acp-15-13453-2015, 2015.

342 Cappa, C. D., Lim, C. Y., Hagan, D. H., Coggon, M., Koss, A., Sekimoto, K., de Gouw, J., Onasch, T. B., Warneke,
343 C., and Kroll, J. H.: Biomass-burning-derived particles from a wide variety of fuels – Part 2: Effects of
344 photochemical aging on particle optical and chemical properties, *Atmos. Chem. Phys.*, 20, 8511-8532,
345 doi:10.5194/acp-20-8511-2020, 2020.

346 Chand, D., Wood, R., Anderson, T. L., Sathesh, S. K., and Charlson, R. J.: Satellite-derived direct radiative effect of
347 aerosols dependent on cloud cover, *Nat. Geosci.*, 2, 181-184, doi:10.1038/Ngeo437, 2009.

348 China, S., Mazzoleni, C., Gorkowski, K., Aiken, A. C., and Dubey, M. K.: Morphology and mixing state of individual
349 freshly emitted wildfire carbonaceous particles, *Nat. Commun.*, 4:2122 doi: 10.1038/ncomms3122, 2013.

350 Costantino, L., and Bréon F. M.: Aerosol indirect effect on warm clouds over South-East Atlantic from co-located
351 MODIS and CALIPSO observations, *Atmos. Chem. Phys.*, 13, 69-88, doi:10.5194/acp-13-69-2013, 2013.

352 Das, S., Harshvardhan, H., and Colarco, P. R.: The influence of elevated smoke layers on stratocumulus clouds over
353 the SE Atlantic in the NASA Goddard Earth Observing System (GEOS) Model, *J. Geophys. Res. Atmos.*, 125,
354 e2019JD031209, doi:10.1029/2019JD031209, 2020.

355 Diamond, M. S., Dobraki, A., Freitag, S., Small Griswold, J. D., Heikkila, A., Howell, S. G., Kacarab, M. E.,
356 Podolske, J. R., Saide, P. E., and Wood, R.: Time-dependent entrainment of smoke presents an observational
357 challenge for assessing aerosol–cloud interactions over the southeast Atlantic Ocean, *Atmos. Chem. Phys.*, 18,
358 14623-14636, <https://doi.org/10.5194/acp-18-14623-2018>, 2018.

359 Doherty, S. J., Saide, P. E., Zuidema, P., Shinozuka, Y., Ferrada, G. A., Gordon, H., Mallet, M., Meyer, K.,
360 Painemal, D., Howell, S. G., Freitag, S., Dobraki, A., Podolske, J. R., Burton, S. P., Ferrare, R. A., Howes, C.,
361 Nabat, P., Carmichael, G. R., da Silva, A., Pistone, K., Chang, I., Gao, L., Wood, R., and Redemann, J.: Modeled
362 and observed properties related to the direct aerosol radiative effect of biomass burning aerosol over the Southeast
363 Atlantic, *Atmos. Chem. Phys.*, 22, 1-46, <https://doi.org/10.5194/acp-22-1-2022>, 2022.

364 Gordon, H., Field, P. R., Abe, S. J., Dalvi, M., Grosvenor, D. P., Hill, A. A., Johnson, B. T., Miltenberger, A. K.,
365 Yoshioka, M., and Carslaw, K. S.: Large simulated radiative effects of smoke in the south-east Atlantic, *Atmos.
366 Chem. Phys.*, 18, 15261-15289, doi:10.5194/acp-18-15261-2018, 2018.

367 Grund, C. J., and Eloranta, E. W.: University of Wisconsin high spectral resolution lidar, *Opt. Eng.*, 30, 6-12, 1991.

368 Gupta, S., McFarquhar, G. M., O'Brien, J. R., Poellot, M. R., Delene, D. J., Miller, R. M., and Small Griswold, J. D.:
369 Precipitation Susceptibility of Marine Stratocumulus with Variable Above and Below-Cloud Aerosol
370 Concentrations over the Southeast Atlantic, *Atmos. Chem. Phys. Discuss. [preprint]*, <https://doi.org/10.5194/acp-2021-677>, in review, 2021.

371 Hair, J. W., Hostettler, C. A., Cook, A. L., Harper, D. B., Ferrare, R. A., Mack, T. L., Welch, W., Izquierdo, L. R.,
372 Hovis, F. E.: Airborne High Spectral Resolution Lidar for profiling aerosol optical properties, *Appl. Optics*, 47, doi:
373 10.1364/AO.47.006734, 2008.

374

375 Haywood, J. M., Osborne, S. R., Francis, P. N., Keil, A., Formenti, P., Andreae, M. O., and Kaye, P. H.: The mean
 376 physical and optical properties of regional haze dominated by biomass burning aerosol measured from the C-130
 377 aircraft during SAFARI 2000, *J. Geophys. Res.*, **108**, 8473, <https://doi.org/10.1029/2002JD002226>, 2003.

378 Haywood, J. M., Abel, S. J., Barrett, P. A., Bellouin, N., Blyth, A., Bower, K. N., Brooks, M., Carslaw, K., Che, H.,
 379 Coe, H., Cotterell, M. I., Crawford, I., Cui, Z., Davies, N., Dingley, B., Field, P., Formenti, P., Gordon, H., de
 380 Graaf, M., Herbert, R., Johnson, B., Jones, A. C., Langridge, J. M., Malavelle, F., Partridge, D. G., Peers, F.,
 381 Redemann, J., Stier, P., Szpek, K., Taylor, J. W., Watson-Parris, D., Wood, R., Wu, H., and Zuidema, P.: The
 382 CLoud–Aerosol–Radiation Interaction and Forcing: Year 2017 (CLARIFY-2017) measurement campaign, *Atmos.*
 383 *Chem. Phys.*, **21**, 1049–1084, <https://doi.org/10.5194/acp-21-1049-2021>, 2021.

384 Kacarab, M., Thornhill, K. L., Dobraki, A., Howell, S. G., O'Brien, J. R., Freitag, S., Poellot, M. R., Wood, R.,
 385 Zuidema, P., Redemann, J., and Nenes, A.: Biomass burning aerosol as a modulator of the droplet number in the
 386 southeast Atlantic region, *Atmos. Chem. Phys.*, **20**, 3029–3040, <https://doi.org/10.5194/acp-20-3029-2020>, 2020.

387 Keil, A., and Haywood, J. M.: Solar radiative forcing by biomass burning aerosol particles during SAFARI 2000: A
 388 case study based on measured aerosol and cloud properties, *J. Geophys. Res. Atmos.*, **108**, 8467,
 389 doi:10.1029/2002JD002315, 2003.

390 Klopfer, D., Formenti, P., Namwoonde, A., Cazaunau, M., Chevallier, S., Feron, A., Gaimoz, C., Hease, P., Lahmidi,
 391 F., Mirande-Bret, C., Triquet, S., Zeng, Z., and Piketh, S. J.: Chemical composition and source apportionment of
 392 atmospheric aerosols on the Namibian coast, *Atmos. Chem. Phys.*, **20**, 15,811–15,833, doi:10.5194/acp-20-15811-
 393 2020, 2020.

394 Koch, D., and Del Genio A. D.: Black carbon semi-direct effects on cloud cover: review and synthesis, *Atmos. Chem.*
 395 *Phys.*, **10**, 7685–7696, doi:10.5194/acp-10-7685-2010, 2010.

396 Lu, Z., Liu, X., Zhang, Z., Zhao, C., Meyer, K., Rajapakshe, C., Wu, C., Yang, Z., and Penner, J.: Biomass smoke
 397 from southern Africa can significantly enhance the brightness of stratocumulus over the southeastern Atlantic
 398 Ocean, *Proc. Natl. Acad. Sc.*, **115**, 2924–2929, doi:10.1073/pnas.1713703115, 2018.

399 Mallet, M., Solmon, F., Nabat, P., Elguindi, N., Waquet, F., Bouniol, D., Sayer, A. M., Meyer, K., Roehrig, R.,
 400 Michou, M., Zuidema, P., Flaaant, C., Redemann, J., and Formenti, P.: Direct and semi-direct radiative forcing of
 401 biomass-burning aerosols over the southeast Atlantic (SEA) and its sensitivity to absorbing properties: a regional
 402 climate modeling study, *Atmos. Chem. Phys.*, **20**, 13191–13216, <https://doi.org/10.5194/acp-20-13191-2020>, 2020.

403 McFarquhar, G. M., and Wang, H.: Effects of aerosols on trade wind cumuli over the Indian Ocean: Model
 404 simulations, *Q. J. R. Meteorol. Soc.*, **132**, 821–843, doi:10.1256/qj.04.179, 2006.

405 Mechoso, C. R., Wood, R., Weller, R., Bretherton, C. S., Clarke, A. D., Coe, H., Fairall, C., Farrar, J. T., Feingold,
 406 G., Garreaud, R., Grados, C., McWilliams, J., de Szoeme, S. P., Yuter, S. E., and Zuidema, Z.: Ocean–cloud–
 407 atmosphere–land interactions in the Southeastern Pacific: The VOCALS program, *B. Am. Meteorol. Soc.*, **95**, 357–
 408 375, doi:10.1175/BAMS-D-11-00246.1, 2013.

409 Meyer, K., Platnick, S., Oreopoulos, L., and Lee, D.: Estimating the direct radiative effect of absorbing aerosols
 410 overlying marine boundary layer clouds in the southeast Atlantic using MODIS and CALIOP, *J. Geophys. Res.*
 411 *Atmos.*, **118**, 4801–4815, doi:10.1002/jgrd.50449, 2013.

412 Müller, D., Wandinger, U., and Ansmann, A.: Microphysical particle parameters from extinction and backscatter lidar
 413 data by inversion with regularization: theory, *Appl. Optics*, **38**, 2346–2357, 1999a.

414 Müller, D., Wandinger, U., and Ansmann, A.: Microphysical particle parameters from extinction and backscatter lidar
 415 data by inversion with regularization: simulation, *Appl. Optics*, **38**, 2358–2368, 1999b.

416 Müller, D., Hostetler, C. A., Ferrare, R. A., Burton, S. P., Chemeyakin, E., Kolgotin, A., Hair, J. W., Cook, A. L.,
 417 Harper, D. B., Rogers, R. R., Hare, R. W., Cleckner, C. S., Oblad, M. D., Tomlinson, J., Berg, L. K., and Schmid,
 418 B.: Airborne multiwavelength high spectral resolution lidar (HSRL-2) observations during TCAP 2012: vertical
 419 profiles of optical and microphysical properties of a smoke/urban haze plume over the northeastern coast of the US,
 420 *Atmos. Meas. Tech.*, **7**, 3487–3496, doi:10.5194/amt-7-3487-2014, 2014.

421 Müller, D., Chemeyakin, E., Kolgotin, A., Ferrare, R. A., Hostetler, C. A., and Romanov, A.: Automated, unsupervised,
 422 inversion of multiwavelength lidar data with TiARA: assessment of retrieval performance of microphysical
 423 parameters using simulated data, *Appl. Optics*, **58**, 4981–5007, doi:10.1364/AO.58.004981, 2019.

424 Painemal, D., Kato, S., and Minnis, P.: Boundary layer regulation in the southeast Atlantic cloud microphysics during
 425 the biomass burning season as seen by the A-train satellite constellation, *J. Geophys. Res. Atmospheres*, **119**,
 426 11,288–211,302, doi:10.1002/2014JD022182, 2014.

427 Peers, F., Francis, P., Fox, C., Abel, S. J., Szpek, K., Cotterell, M. I., Davies, N. W., Langridge, J. M., Meyer, K. G.,
 428 Platnick, S. E., and Haywood, J. M.: Observation of absorbing aerosols above clouds over the south-east Atlantic
 429 Ocean from the geostationary satellite SEVIRI – Part 1: Method description and sensitivity, *Atmos. Chem. Phys.*,
 430 **19**, 9595–9611, <https://doi.org/10.5194/acp-19-9595-2019>, 2019.

431 Penner, J. E., Zhang, S. Y., and Chuang, C. C.: Soot and smoke aerosol may not warm climate, *J. Geophys. Res. Atmospheres*, 108, 4657, doi:10.1029/2003JD003409, 2003.

432 Pistone, K., Zuidema, P., Wood, R., Diamind, M., da Silva, A. M., Ferrada, G., Saide, P. E., Ueyama, R., Ryoo, J.-M., Pfister, L., Podolske, J., Noone, D., Bennett, R., Stith, E., Carmichael, G., Redemann, J., Flynn, C., LeBlanc, S., Segal-Rozenhaimer, M., and Shinozuka, Y.: Exploring the elevated water vapor signal associated with the free tropospheric biomass burning plume over the southeast Atlantic Ocean, *Atmos. Chem. Phys.*, 21, 9643-9668, <https://doi.org/10.5194/acp-21-9643-2021>, 2021.

433 Pósfai, M., Simonics, R., Li, J., Hobbs, P. V., and Buseck, P. R.: Individual aerosol particles from biomass burning in 434 southern Africa: 1. Compositions and size distributions of carbonaceous particles, *J. Geophys. Res.*, 108, 8483, 435 doi:10.1029/2002JD002291, 2003.

436 Ramanathan, V., Crutzen, P. J., Kiehl, J. T., and Rosenfeld, D.: Aerosols, climate, and the hydrological cycle, *Science*, 437 294(5549), 2119-2124, doi:10.1126/science.1064034, 2001.

438 Randles, C.A., daSilva, A. M., Buchard, V., Colarco, P. R., Darmenov, A., Govindaraju, P., Smirnov, A., Holben, B., 439 Ferrare, R. A., Hair, J., Shinozuka, Y., and Flynn, C. J.: The MERRA-2 aerosol reanalysis, 1980 onward. Part I: 440 System description and data assimilation evaluation, *J. Climate*, 30, 6823–6850, doi: 10.1175/JCLI-D-16-0609.1, 441 2017.

442 Redemann, J., Wood, R., Zuidema, P., Doherty, S. J., Luna, B., LeBlanc, S. E., Diamond, M. S., Shinozuka, Y., Chang, 443 I. Y., Ueyama, R., Pfister, L., Ryoo, J.-M., Dobracki, A. N., da Silva, A. M., Longo, K. M., Kacenelenbogen, M. 444 S., Flynn, C. J., Pistone, K., Knox, N. M., Pike, S. J., Haywood, J. M., Formenti, P., Mallet, M., Stier, P., 445 Ackerman, A. S., Bauer, S. E., Fridlind, A. M., Carmichael, G. R., Saide, P. E., Ferrada, G. A., Howell, S. G., 446 Freitag, S., Cairns, B., Holben, B. N., Knobelspiesse, K. D., Taneli, S., L'Ecuyer, T. S., Dzambo, A. M., Sy, O. O., 447 McFarquhar, G. M., Poellot, M. R., Gupta, S., O'Brien, J. R., Nenes, A., Kacarab, M., Wong, J. P. S., Small- 448 Griswold, J. D., Thornhill, K. L., Noone, D., Podolske, J. R., Schmidt, K. S., Pilewskie, P., Chen, H., Cochrane, S. 449 P., Sedlacek, A. J., Lang, T. J., Stith, E., Segal-Rozenhaimer, M., Ferrare, R. A., Burton, S. P., Hostetler, C. A., 450 Diner, D. J., Seidel, F. C., Platnick, S. E., Myers, J. S., Meyer, K. G., Spangenberg, D. A., Maring, H., and Guo, L.: 451 An overview of the ORACLES (ObseRvations of Aerosols above Clouds and their intEractionS) project: aerosol- 452 cloud-radiation interactions in the southeast Atlantic basin, *Atmos. Chem. Phys.*, 21, 1507-1563, doi:10.5194/acp- 453 21-1507-2021, 2021.

454 Rogers, R. R., Hair, J. W., Hostetler, C. A., Ferrare, R. A., Obland, M. D., Cook, A. L., Harper, D. B., Burton, S. P., 455 Shinozuka, Y., McNaughton, C. S., Clarke, A. D., Redemann, J., Russell, P. B., Livingston, J. M., and Kleinman, 456 L. I.: NASA LaRC airborne high spectral resolution lidar aerosol measurements during MILAGRO: observations 457 and validation, *Atmos. Chem. Phys.*, 9, 4811-4826, 2009.

458 Ryoo, J.-M., Pfister, L., Ueyama, R., Zuidema, P., Wood, R., Chang, I., and Redemann, J.: A meteorological 459 overview of the ORACLES (ObseRvations of Aerosols above CLouds and their intEractionS) campaign over the 460 southeastern Atlantic during 2016–2018: Part 1 – Climatology, *Atmos. Chem. Phys.*, 21, 16689–16707, 461 <https://doi.org/10.5194/acp-21-16689-2021>, 2021.

462 Sakaeda, N., Wood, R., and Rasch, P. J.: Direct and semidirect aerosol effects of southern African biomass burning 463 aerosol, *J. Geophys. Res. Atmospheres*, 116, D12205, doi:10.1029/2010JD015540, 2011.

464 Sawamura, P., Moore, R. H., Burton, S. P., Chemyakin, E., Müller, D., Kolgotin, A., Ferrare, R. A., Hostetler, C. A., 465 Ziembka, L. D., Beyersdorf, A. J., and Anderson, B. E.: HSRL-2 aerosol optical measurements and microphysical 466 retrievals vs. airborne in situ measurements during DISCOVER-AQ 2013: an intercomparison study, *Atmos. Chem. 467 Phys.*, 17, 7229-7243, doi.org/10.5194/acp-17-7229-2017, 2017.

468 Schmid, B., Ferrare, R. A., Flynn, C., Elleman, R., Covert, D., Strawa, A., Welton, E., Turner, D., Jonsson, H., 469 Redemann, J., Eilers, J., Ricci, K., Hallar, A. G., Clayton, M., Michalsky, J., Smirnov, A., Holben, B., and Barnard, 470 J. : How well do state-of-the-art techniques measuring the vertical profile of tropospheric aerosol extinction 471 compare? *J. Geophys. Res.*, 111, D05S07, doi:10.1029/2005JD005837, 2006.

472 She, C. Y., Alvarez II, R. J., Caldwell, L. M., and Krueger, D. A.: High-spectral-resolution Rayleigh-Mie lidar 473 measurement of aerosol and atmospheric profiles, *Opt. Lett.*, 17, 541-543, 1992.

474 **Shingler, T., Crosbie, E., Ortega, A., Shiraiwa, M., Zuend, A., Beyersdorf, A., Ziembka, L., Anderson, B., Thornhill, 475 L., Perring, A. E., Schwarz, J. P., Campazano-Jost, P., Day, D. A., Jimenez, J. L., Hair, J. W., Mikoviny, T., 476 Wisthaler, A., & Sorooshian, A.: Airborne characterization of subsaturated aerosol hygroscopicity and dry refractive 477 index from the surface to 6.5km during the SEAC⁴RS campaign, *J. Geophys. Res.*, 121(8), 4188-4210,** 478 <https://doi.org/10.1002/2015JD024498>, 2016.

479 Shinozuka, Y., Saide, P. E., Ferrada, G. A., Burton, S. P., Ferrare, R. A., Doherty, S. J., Gordon, H., Longo, K., Mallet, 480 M., Feng, Y., Wang, Q., Cheng, Y., Dobracki, A., Freitag, S., Howell, S. G., LeBlanc, S., Flynn, C., Segal- 481 Rozenhaimer, M., Pistone, K., Podolske, J. R., Stith, E. J., Bennett, J. R., Carmichael, G. R., da Silva, A., 482

483 Formatted: Font: Not Italic

487 Govindaraju, R., Leung, R., Zhang, Y., Pfister, L., Ryoo, J.-M., Redemann, J., Wood, R., and Zuidema, P.: Modeling
 488 of the smoky troposphere of the southeast Atlantic: a comparison to ORACLES airborne observations from
 489 September of 2016, *Atmos. Chem. Phys.*, 20, 11491-11526, doi:10.5194/acp-20-11491-2020, 2020.

490 Shipley, S. T., Tracy, D. H., Eloranta, E. W., Tauger, J. T., Stroga, J. T., Roesler, F. L., and Weinman, J. A.: High
 491 spectral resolution lidar to measure optical scattering properties of atmospheric aerosols. 1. Theory and
 492 instrumentation, *Appl. Optics*, 22, 3716-3724, 1983.

493 Stein, A.F., Draxler, R. R., Rolph, G. D., Stunder, B. J. B., Cohen, M. D., and Ngan, F.: NOAA's HYSPLIT
 494 atmospheric transport and dispersion modeling system, *B. Am. Meteorol. Soc.*, 96, 2059-2077, doi:10.1175/BAMS-
 495 D-14-00110.1, 2015.

496 Veselovskii, I., Kolgotin, A., Grazianov, V., Müller, D., Wandinger, U., and Whiteman, D. N.: Inversion with
 497 regularization for the retrieval of tropospheric aerosol parameters from multi-wavelength lidar sounding, *Appl.*
 498 *Optics*, 41, 3685-3699, 2002.

499 Wilcox, E. M.: Stratocumulus cloud thickening beneath layers of absorbing smoke aerosol, *Atmos. Chem. Phys.*, 10,
 500 11769-11777, doi:10.5194/acp-10-11769-2010, 2010.

501 Wilcox, E. M.: Direct and semi-direct radiative forcing of smoke aerosols over clouds, *Atmos. Chem. Phys.*, 12, 139-
 502 149, doi:10.5194/acp-12-139-2012, 2012.

503 Wu, H., Taylor, J. W., Szpek, K., Langridge, J. M., Williams, P. I., Flynn, M., Allan, J. D., Abel, S. J., Pitt, J., Cotterell,
 504 M. I., Fox, C., Davies, N. W., Haywood, J., and Coe, H.: Vertical variability of the properties of highly aged biomass
 505 burning aerosol transported over the southeast Atlantic during CLARIFY-2017, *Atmos. Chem. Phys.*, 20, 12697-
 506 12719, <https://doi.org/10.5194/acp-20-12697-2020>, 2021.

507 Xu, F., Gao, L., Redemann, J., Flynn, C.J., Espinosa, W.R., da Silva, A.M., Starnes, S., Burton, S.P., Liu, X., Ferrare,
 508 R., Cairns, B., and Dubovik, O.: A Combined Lidar-Polarimeter Inversion Approach for Aerosol Remote Sensing
 509 Over Ocean, *Front. Remote Sens.*, 2:620871, doi: 10.3389/frsen.2021.620871, 2021.

510 Yamaguchi T, Feingold, G., Kazil, J., and McComiskey, A.: Stratocumulus to cumulus transition in the presence of
 511 elevated smoke layers. *Geophys. Res. Lett.*, 42: 10478-10485, 2015.

512 Zhang, J. and Zuidema, P.: The diurnal cycle of the smoky marine boundary layer observed during August in the
 513 remote southeast Atlantic, *Atmos. Chem. Phys.*, 19, 14493-14516, <https://doi.org/10.5194/acp-19-14493-2019>,
 514 2019.

515 Zhang, Z., Meyer, K., Yu, H., Platnick, S., Colarco, P. R., Liu, Z., and Oreopoulos, L.: Shortwave direct radiative
 516 effects of above-cloud aerosols over global oceans derived from 8 years of CALIPSO and MODIS observations,
 517 *Atmos. Chem. Phys.*, 16, 2877-2900, doi:10.5194/acp-16-2877-2016, 2016.

518 Zhang, X., Mao, M., Yin, Y., and Tang, S.: The absorption Ångström exponent of black carbon with brown coatings:
 519 effects of aerosol microphysics and parameterization, *Atmos. Chem. Phys.*, 20, 9701-9711, doi:10.5194/acp-20-
 520 9701-2020, 2020.

521 Zuidema, P., Redemann, J., Haywood, J., Wood, R., Piketh, S., Hipondoka, M., and Formenti, P.: Smoke and clouds
 522 above the southeast Atlantic, *B. Am. Meteorol. Soc.*, 97, 1131-1135, doi:10.1175/BAMS-D-15-00082.1, 2016.

523 Zuidema, P., Sedlacek III, A. J. Flynn, C., Springston, S., Delgadillo, R., Zhang, J., Aiken, A. C., Koontz, A., and
 524 Muradyan, P.: The Ascension Island boundary layer in the remote Southeast Atlantic is often smoky, *Geophys. Res.*
 525 *Lett.*, 45, 4456-4465, doi:10.1002/2017/GL076926, 2018.

Formatted: Font: Not Italic

Formatted: Font: 10 pt

Formatted: Indent: Left: 0", Hanging: 0.13"

Formatted: Font: 10 pt

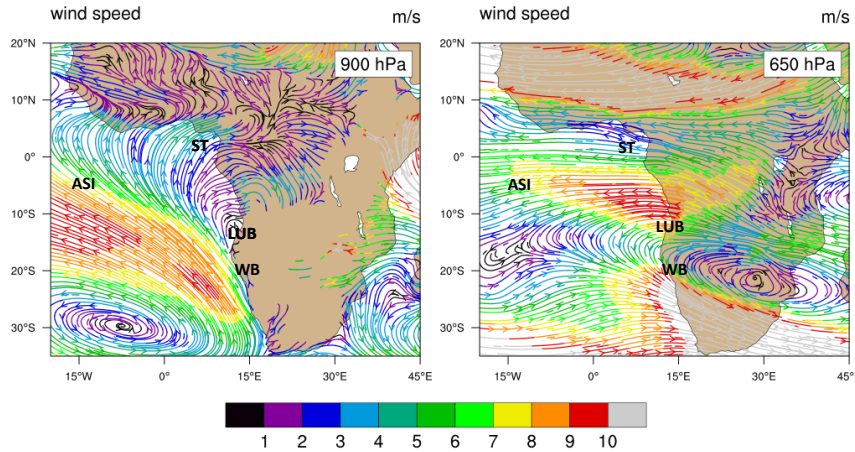
Deleted: ¶

528
529
530

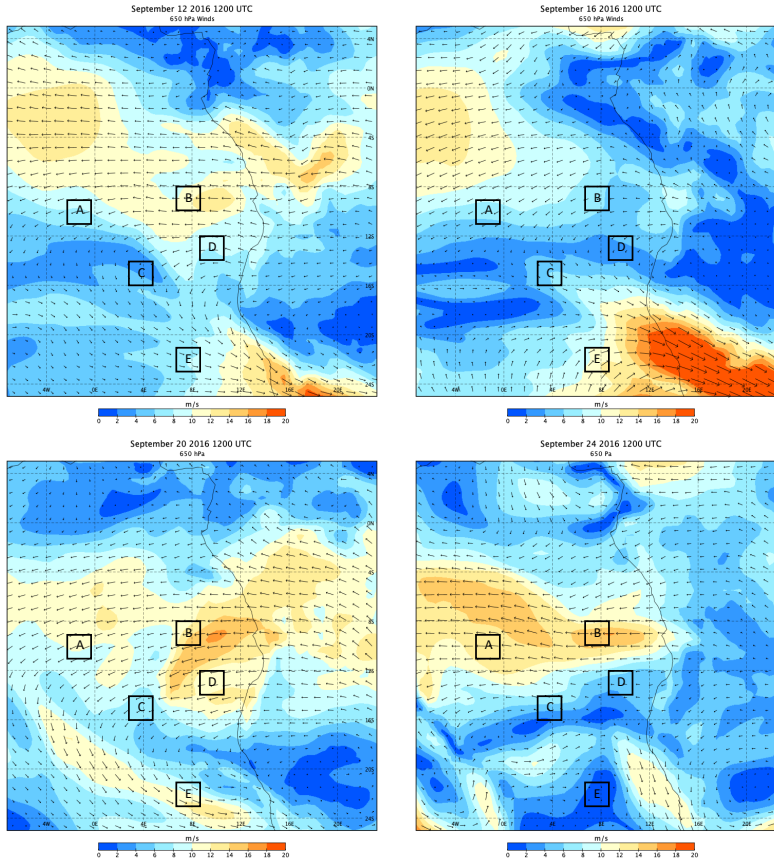
Table 1: Averaging area, flight time periods, the duration over water and number of HYSPLIT backward trajectories, and number of HSRL-2 profiles in each grid box used in the study.

Box	Averaging Area	Averaging Days	Time of Day	Duration in Hours Over Water at 3.5 km	Number of Profiles
A	11° S-9° S; 1° W-1° E	9/12,16	11:00 UTC	44.3±7.0 (N = 19)	50
B	10° S-8° S; 8° E-10° E	9/12,16,18	10:00 UTC	14.9±4.5 (N = 27)	56
C	16° S-14° S; 4° E-6° E	9/12,16	13:00 UTC	40.4±7.2 (N = 19)	51
D	14° S-12° S; 10° E-12° E	9/18,24	09:00 UTC	5.5±2.0 (N = 27)	46
E	23° S-21° S; 8° E-10° E	9/20,22	14:00 UTC	-	36

531

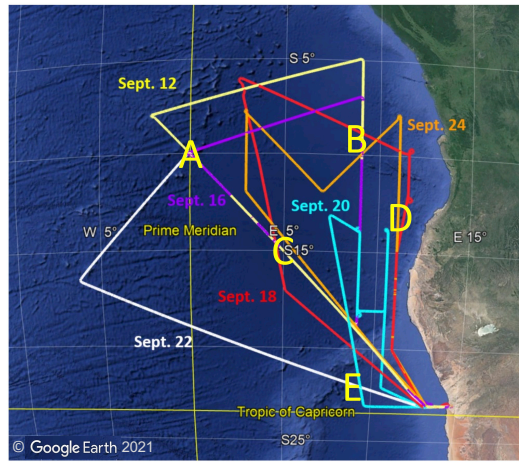


533
 534 **Figure 1:** MERRA2 monthly mean reanalysis of 900 and 650 hPa streamlines for September 2016. Stations marked
 535 are Ascension Island (ASI), Lubango (LUB), a long-term AERONET site at 2 km elevation, and Walvis Bay (WB),
 536 where ER-2 flights originated from during the September 2016 ORACLES IOP. Flights in August 2017 and
 537 September/October 2018 originated from São Tomé (ST).
 538



539
 540 **Figure 2:** MERRA2 reanalysis of 650 hPa winds at 1200 UTC on September 12, 16, 20, 24, 2016. Grid boxes in the
 541 study are marked with letters.
 542

543
544

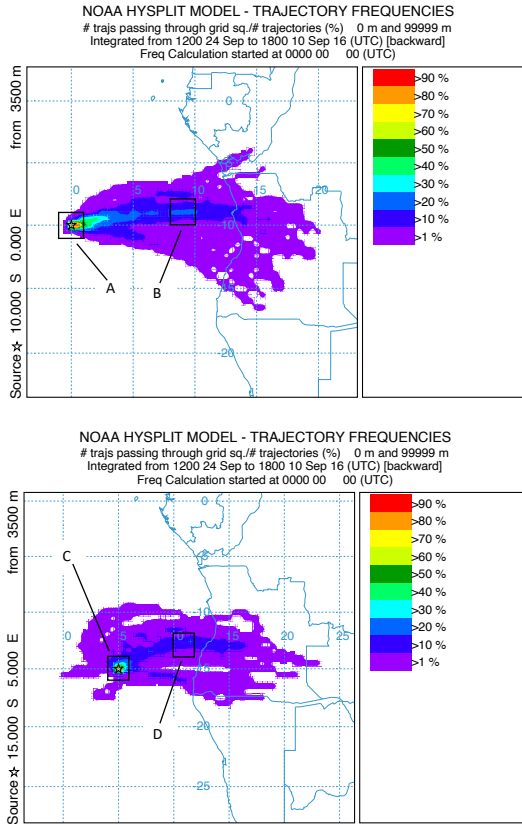


545
546

547
548
549

Figure 3: HSRL-2 science data flight tracks during the September 2016 IOP. Letters refer. to the grid boxes identified in Fig. 2

550



551
552
553
554
555
556

Figure 4: Frequency distribution of 48-hour backward trajectories of air parcels arriving at 3500 m above the centers of grid boxes A and C over the time period of the campaign. Grid boxes B and D are upstream of grid boxes A and C, respectively.

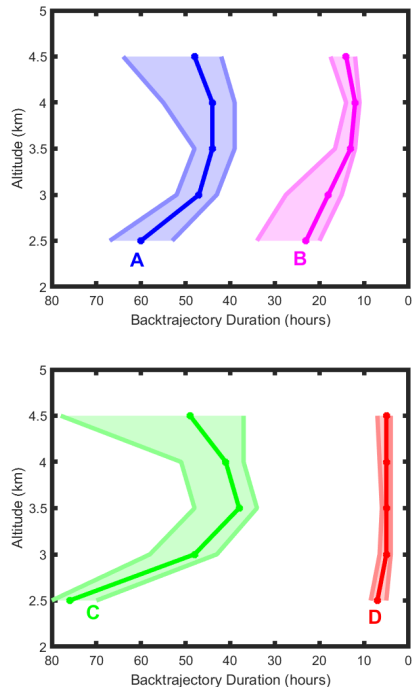
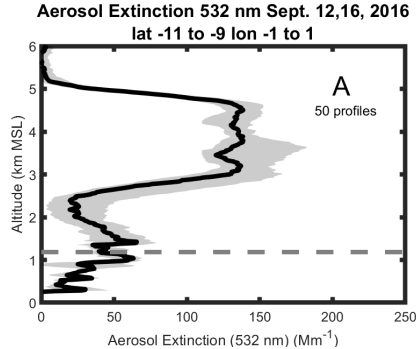
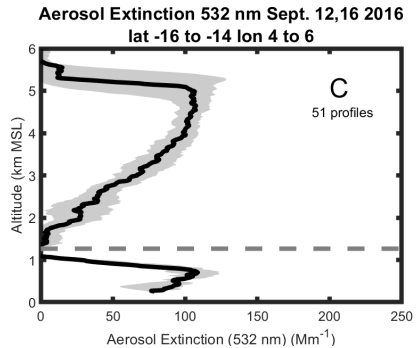


Figure 5: Duration of time spent over water of air parcels arriving at grid boxes marked on the figure. Solid lines are median values, and the shaded portion are the range of the 75th and 25th percentile. The number of trajectories used for the calculation are in Table 1. Trajectory hours are shown in reverse to correspond to the map in Fig. 4.

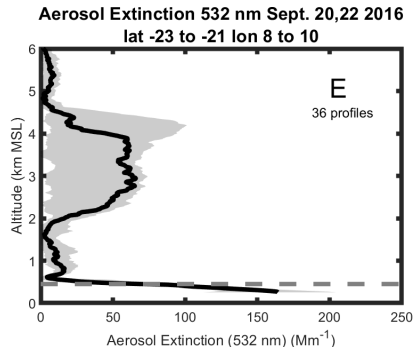
565



566



567



568

569

570

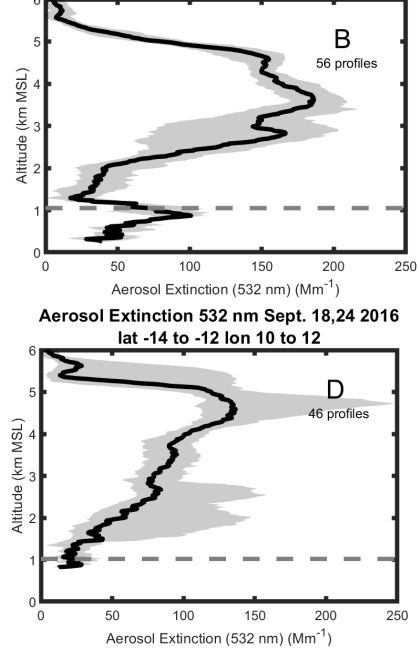
571

572

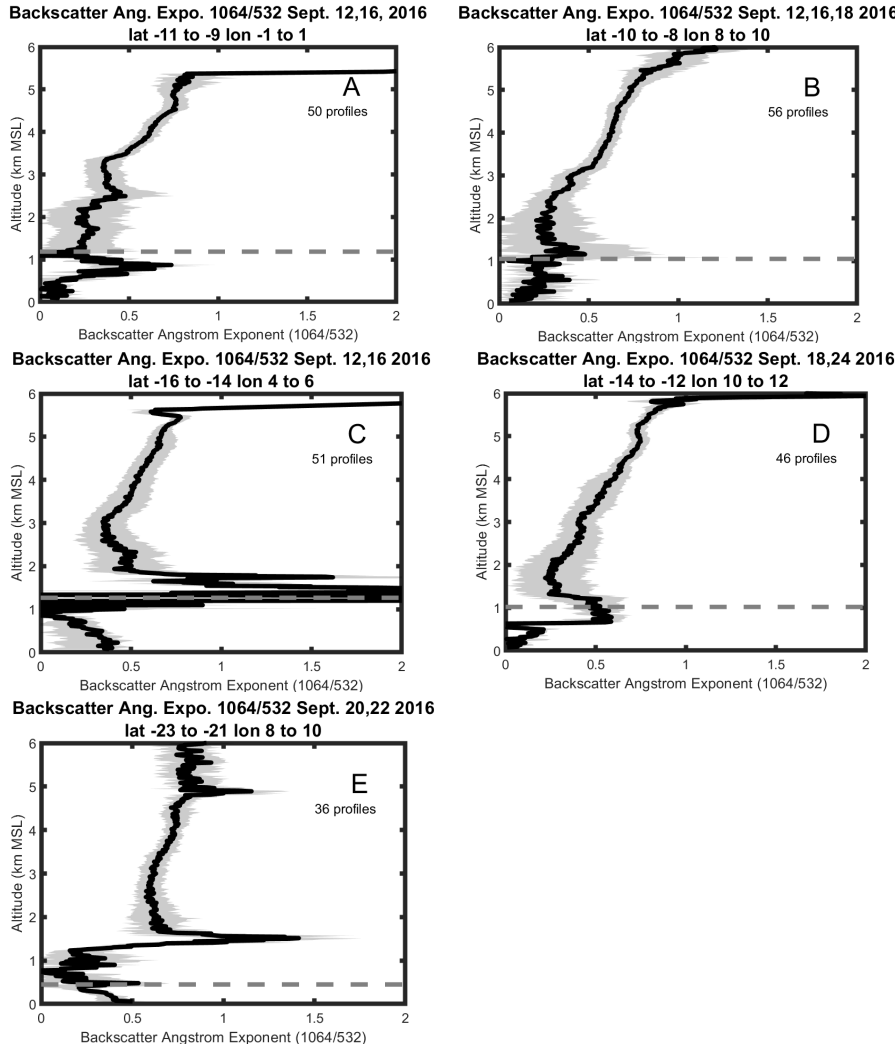
573

574

Aerosol Extinction 532 nm Sept. 12,16,18 2016
lat -10 to -8 lon 8 to 10
56 profiles



575



576

577

578

579

580

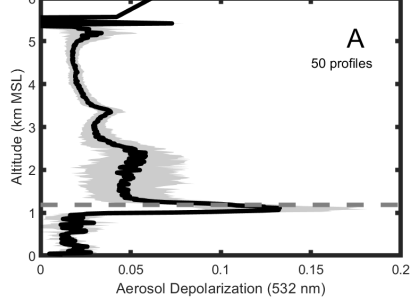
581

582

Figure 7: As in Fig. 6 but for the Wavelength Dependent Backscatter Ångström exponent between 1064 and 532 nm.

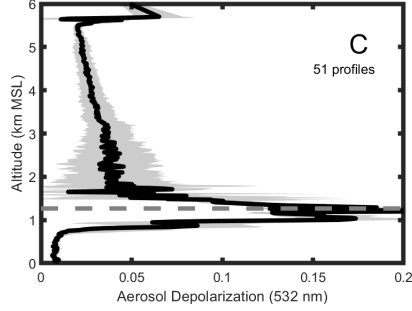
583

Aerosol Depolarization 532 nm Sept. 12,16, 2016
lat -11 to -9 lon -1 to 1



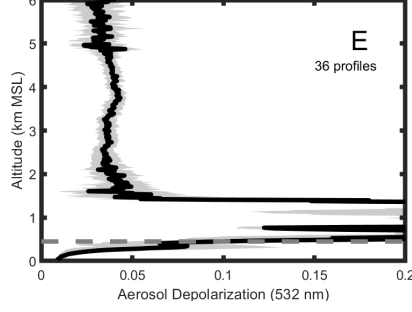
584

Aerosol Depolarization 532 nm Sept. 12,16 2016
lat -16 to -14 lon 4 to 6



585

Aerosol Depolarization 532 nm Sept. 20,22 2016
lat -23 to -21 lon 8 to 10



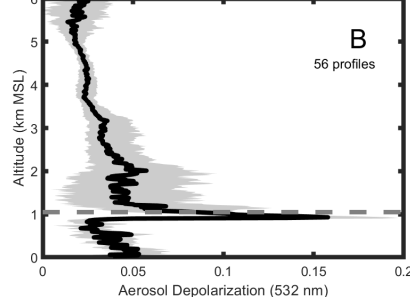
586

587

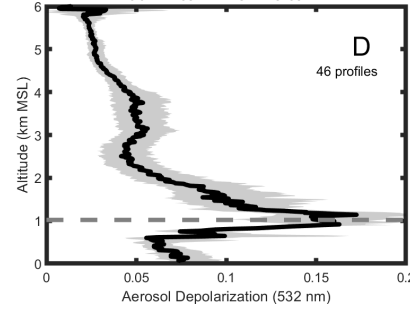
588

589

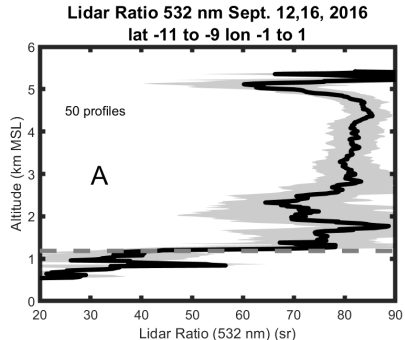
Aerosol Depolarization 532 nm Sept. 12,16,18 2016
lat -10 to -8 lon 8 to 10



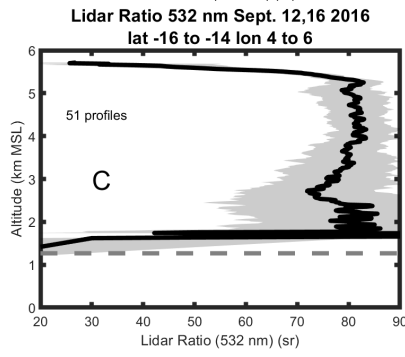
Aerosol Depolarization 532 nm Sept. 18,24 2016
lat -14 to -12 lon 10 to 12



590



591



592

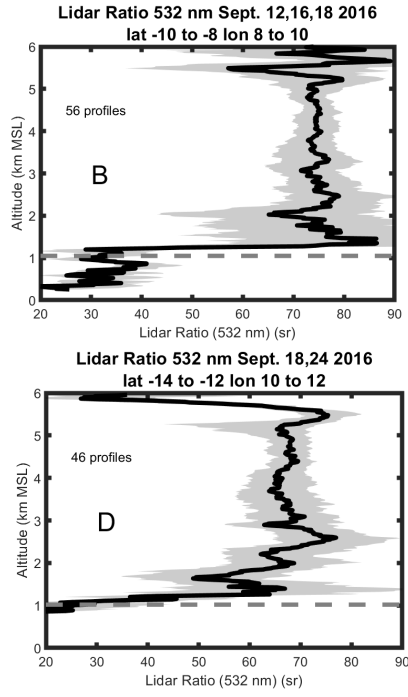
593
594
595
596

Figure 9: As in Fig. 6 but for the Lidar Ratio at 532 nm.

597

598

599
600
601
602
603
604
605
606

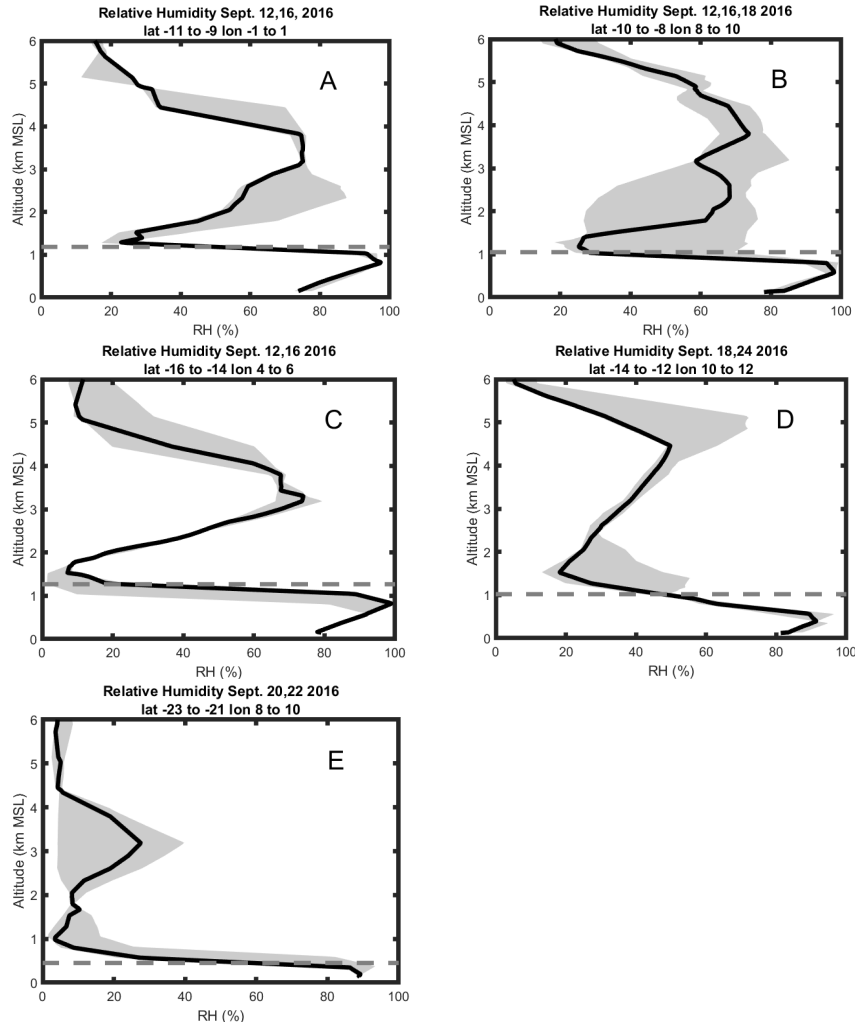


Figure 10: Relative Humidity (%) in grid boxes A (upper left), B (upper right), C (middle left), D (middle right) and E (lower left) from MERRA2 reanalysis corresponding to the HSRL-2 profiles shown in Figs. 6-9. The dark line represents the median value and grey shades contain the 25th to 75th percentiles. Dashed line refers to the mean cloud top height.

607

608

609

610

611

612

613

614

615

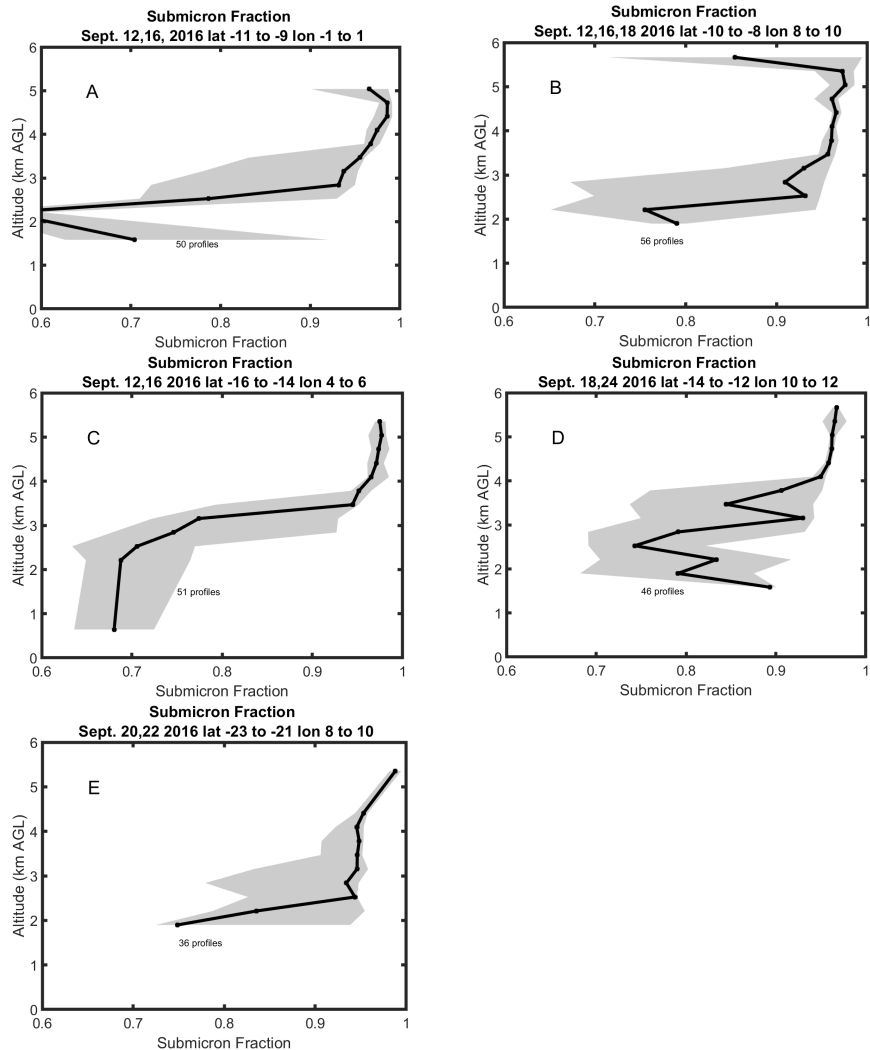


Figure 11: Average vertical profiles of the submicron fraction in grid boxes A (upper left), B (upper right), C (middle left), D (middle right) and E (lower left). The averaging area, dates of flights and total number of one-minute profiles in the average are also shown. The dark line represents the median value and grey shades contain the 25th to 75th percentiles.

616

617

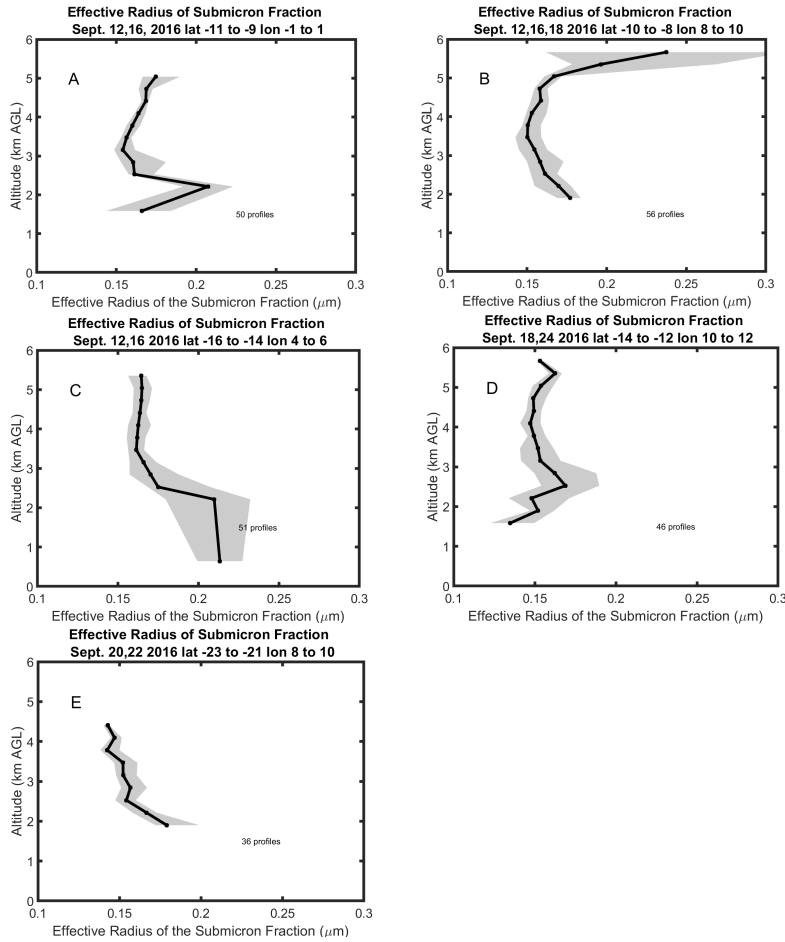
618
619
620

Figure 12: As in Fig. 11 but for the effective radius of the submicron fraction.